

Superposition of Fragment Excitations for Excited States of Large Clusters with Application to Helium Clusters

Kristina D. Closser,^{†,‡,§} Qinghui Ge,^{†,‡} Yuezhi Mao,[†] Yihan Shao,[¶] and Martin Head-Gordon^{*,†,‡}

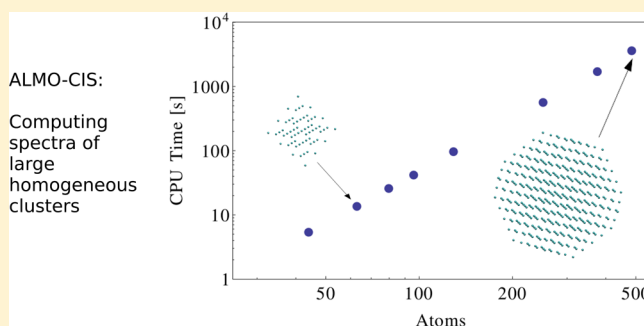
[†]Kenneth S. Pitzer Center for Theoretical Chemistry, Department of Chemistry, University of California, Berkeley, California 94720, United States

[‡]Chemical Sciences Division, Lawrence Berkeley National Laboratory, Berkeley, California 94720, United States

[¶]Q-Chem, Inc., 6601 Owens Drive, Suite 105, Pleasanton, California 94588, United States

Supporting Information

ABSTRACT: We develop a local excited-state method, based on the configuration interaction singles (CIS) wave function, for large atomic and molecular clusters. This method exploits the properties of absolutely localized molecular orbitals (ALMOs), which strictly limits the total number of excitations, and results in formal scaling with the third power of the system size for computing the full spectrum of ALMO–CIS excited states. The derivation of the equations and design of the algorithm are discussed in detail, with particular emphasis on the computational scaling. Clusters containing ~500 atoms were used in evaluating the scaling, which agrees with the theoretical predictions, and the accuracy of the method is evaluated with respect to standard CIS. A pioneering application to the size dependence of the helium cluster spectrum is also presented for clusters of 25–231 atoms, the largest of which results in the computation of 2310 excited states per sampled cluster geometry.



1. INTRODUCTION

Predicting the electronically excited states of large systems with reasonable accuracy is an ongoing challenge for quantum chemistry. The competition between accuracy and efficiency places significant limitations on the methods that are practically useful.^{1,2} By far, the most widely used method for computing the excited states of medium-sized and larger molecules is time-dependent Kohn–Sham density functional theory (TD-DFT).^{3,4} This method involves computational effort per state, which is similar to the effort required to treat the ground state by DFT. Formally, a quadratic number of variables, akin to single excitations, are involved, and the computational cost typically grows between the square and the cube of system size per state. Thus, calculations of roughly 5–40 states are manageable if the corresponding ground-state calculation is feasible. On the other hand, obtaining *all* excited states requires computational effort that increases asymptotically with the sixth power of molecular size, which rapidly becomes unfeasible, even when the ground-state calculation is tractable. The accuracy of TD-DFT calculations is also limited by the well-known difficulty in systematically improving present-day density functionals. Incorrect asymptotic potentials cause errors in the position of Rydberg excited states, while self-interaction errors yield dramatic failures for charge transfer excited states. To some extent using modern range-separated density functionals remedies these failures.^{2,5–8}

In contrast, wave-function-based approaches to excited states are appealing in that they can be straight-forwardly improved

through incorporation of additional degrees of freedom, typically in the form of higher substitutions through a configuration interaction (CI) wave function. The Brillouin Theorem states that the matrix elements of the variationally optimized mean field Hartree–Fock wave function with all singly substituted configurations are strictly zero. Thus, the simplest CI wave function for excited states is CI in the space of single substitutions (CIS):^{3,9}

$$|\Psi\rangle = \sum_s c_s |\Phi_s\rangle \quad (1)$$

CIS has half the number of degrees of freedom of TD-DFT (identical within the Tamm–Dancoff approximation¹⁰), so its computational cost is roughly comparable. Relative to TD-DFT with commonly available functionals, CIS has the advantage of a correct asymptotic potential and zero self-interaction error. However, it completely neglects dynamic electron correlation, which leads to errors in valence excitation energies that are on the order of 1 eV (the correlation energy for a pair of electrons).

More-sophisticated wave function methods introduce additional complexity to account for electron correlation effects through double and higher substitutions. The simplest methods are perturbative cousins to CIS such as the nondegenerate CIS(D) correction,¹¹ and its quasi-degenerate variants.¹² The latter relate closely to the second-order coupled cluster approximation (CC2),¹³

Received: July 23, 2015

Published: October 22, 2015



which is itself an approximation to full equation of motion coupled-cluster (EOM-CC) theory (e.g., EOM-CCSD, EOM-CCSD(T)).^{14,15} The cost of the additional electron correlation can be as low as fourth order in system size for scaled opposite-spin methods,^{16,17} while it is fifth order for the full perturbative methods,¹¹ and sixth order with complete iterative treatment of the doubles. Iterative triples methods scale with the eighth power of system size. Such steep increases in computational cost with system size place increasingly severe restrictions on the systems that can be successfully treated. Even so, the above methods (including TD-DFT) fail for problems where the ground state is not well approximated by a good single configuration, and these must be addressed by active space methods such as the complete active space self-consistent field method (CAS-SCF) and the corresponding second-order perturbative corrections,^{18,19} or with spin-flipping methods.^{20–22}

Great effort has gone into reducing the computational requirements of electronic structure theory calculations for the ground state from quadratic storage and cubic computation toward linear scaling. As argued by Kohn,²³ the one-particle density matrix that controls the ground-state energy is intrinsically “short-sighted”; therefore, in the large system limit only a linear number of variables are significant. While linear scaling methods for forming the effective Hamiltonian have been widely used since the early 1990s,^{24–26} linear scaling replacements for diagonalization, although extensively developed,²⁷ are not widely applied, primarily because extremely large systems are needed to realize adequate sparsity in real space,²⁸ and the situation is even more challenging in spectral representations.

Linear scaling methods, while less thoroughly developed than those for ground states, have also been proposed for excited states.²⁹ Specifically, there have been formulations of CIS and TD-DFT that are appropriate for linear scaling.^{30,31} Some proof-of-concept implementations and calculations have been reported.^{32–35} However, these methods are not widely used for production calculations at the moment, in part because excited states appear to exhibit substantially greater delocalization than ground states.

Therefore, in systems significantly larger than 100 atoms, but not large enough that rigorous linear scaling is possible, it is necessary to apply additional approximations.³⁶ Exploiting the intrinsic locality in certain types of chromophores has led to the development of incremental, multilayer, and fragmentation-based approaches.^{36–41} Biological systems often fall into this category, and reports of heroic calculations with over 20 000 atoms have been reported.⁴² However, the excited states for these systems were only computed on fragments containing no more than 103 atoms.

Grimme recently published a simplified method based on the Tamm–Dancoff approximation to TD-DFT (sTDA), where he reported results for a 483 atom/6879 basis function system.^{43,44} The two-pronged approach used a Löwdin-monopole basis for the two-electron integrals and a bold truncation of the single excitations to make this feasible. This integral approximation leads to a preferential description of delocalized states, and four global parameters were introduced to reduce some of the systematic error.

Even more recently, Liu and Herbert reported a TD-DFT(MI) method that was applicable to computing the excited states of large clusters.⁴⁵ Conceptually almost identical to the ALMO–CIS method presented here, their work also focuses on computing the excited states of clearly defined chromophores, which couple weakly to surrounding solvent molecules. Although, in principle,

their method is extensible to multiple chromophores, the algorithm is optimized for computing a relatively small number of the excited states. Helmich and Hättig proposed a method based on truncation of the pair natural orbital (PNO) space.^{46,47} Although intriguing, their current implementation is still $O(N^4)$ and not practical for large systems when many states are requested.

Almost all current implementations of CIS and TD-DFT are optimized for computing a handful of the low-lying excited states, and both the linear-scaling and fragment-based methods discussed above for treating larger systems continue in this approach. When dealing with large homogeneous systems, such as atomic and molecular clusters, dense manifolds of states with similar energies must be considered, and thus many states (a full description of at least the bands of interest) are required to connect directly to experimental results. In relation to more typical situations where only a few excited states are required, this increases the scaling of the computational cost by at least one power of system size. Noncovalently bound clusters have generated significant interest as they span the range between the gas phase and bulk limits, and they are useful for investigating fundamental differences between bulk and surface properties.^{48–50}

The excitation energies of rare gas clusters have attracted great interest because of their unique properties. Helium clusters in particular are extremely cold, superfluidic,⁵¹ and, when used as a spectroscopic medium, provide a unique environment that allows rotational resolution of dopant solutes.^{52–55} For the electronic spectrum of undoped clusters, the sharp atomic lines (e.g., $2p$ and $3p$) of the He atom give way to broad blue-shifted peaks in large clusters,⁵⁶ which correspond to bands of excited states. The photoionization dynamics of these clusters have also been the subject of considerable interest.⁵⁷

Here, we report the development of a local excited-state method that can adequately describe large numbers of electronic excited states (as needed to describe the bands) of large atomic and molecular clusters at greatly reduced computational cost. In a 1000-atom cluster, the $n = 2$ band would require a minimum of 4000 states to describe correctly. This situation where the number of states increases with cluster size is one that conventional molecular excited-state codes are quite unsuited to handle, and it introduces an enormous additional prefactor to the computational cost. At the same time, because each atom in such a cluster is identical, there is no obvious locality to the excited states: generally, they may be fully delocalized throughout the cluster. Both of these factors make the development of a viable computational method potentially very challenging.

There is one critically important physical advantage that we exploit to make the problem tractable. We have previously reported on the electronically excited states of small helium clusters using standard configuration interaction singles (CIS).^{58,59} In the $n = 2$ manifold, we determined that the excited states could be interpreted in terms of superpositions of atomic-like excitations.⁵⁸ This is perhaps not too surprising, because of the very high ionization energy of He atoms, and the fact that the electron affinity is negative. This characteristic of the excited states suggests that the states associated with the $2p$ and $3p$ bands may be adequately described as superpositions of atomically localized excitations. Such a model has storage requirements that grow linearly per state, and only quadratically for all states. The computational cost then grows no worse than the cube of the number of atoms to obtain the full spectrum of excitations.

The theory presented here is optimized for clusters consisting of identical fragments, which may be atomic or molecular clusters

(e.g., nitrogen clusters, or even water clusters, may be reasonably well described). The ground states of strongly localized molecular clusters were shown to be quite accurately treated, at greatly reduced computational cost, through the use of absolutely localized molecular orbitals (ALMOs).⁶⁰ The ALMO approximation defines the molecular orbital (MO) coefficient matrix to be block diagonal in the molecules comprising the cluster.^{61–64} Thus, each MO on a given molecule is a superposition of only atomic orbitals (AOs) centered on the same molecule. In addition to accelerating SCF calculations for large systems,⁶⁰ ALMOs have been used for calculating the individual contributions to intermolecular interactions.^{65–68} A direct result of the ALMO approximation is that the ALMOs are nonorthogonal between fragments.

ALMOs are an ideal basis for defining a variant of CIS in which states are defined as superpositions of intrafragment excitations. By allowing excitations only within the orbital space of a given fragment, charge transfer between fragments is prohibited and the number of singly excited states used for the calculation grows linearly with cluster size (for a homogeneous cluster). As a result, much larger clusters can be examined than would otherwise be possible. In this paper, we formulate the theory for this local ALMO–CIS method and discuss an efficient cubic scaling implementation that yields all the ALMO–CIS states via direct diagonalization after constructing the corresponding Hamiltonian. We present benchmarks showing the extent to which ALMO–CIS calculations are faithful to full CIS calculations for helium clusters, with satisfactory results. Timings for the algorithm are presented for helium clusters containing ~500 atoms. We also include initial results using the ALMO–CIS method to explore the size dependence of the excitation spectrum of helium clusters with a more thorough report on these systems to appear in a subsequent publication.

2. THEORY

2.1. Notation. Tensors provide a useful notion for treating nonorthogonal functions, such as the ALMOs. Thus, standard tensor notation is used,^{69,70} where subscripts indicate functions in the covariant (given) basis, and superscripts indicate functions in the (biorthogonal) contravariant space. The Einstein summation convention is also employed, where an index that occurs once covariant and once contravariant implies a sum.

Occupied MOs are denoted as i, j, k , virtual orbitals are denoted as a, b, c , and general orbitals are denoted as p, q, r . ALMOs will be represented using $|\psi\rangle$, and later it will be necessary to form a set of projected ALMOs, which will be distinguished using $|\phi\rangle$ (note that, for occupied orbitals, $|\phi_i\rangle = |\psi_i\rangle$, but for the virtuals, $|\phi_a\rangle \neq |\psi_a\rangle$). AO functions are given by χ_μ , auxiliary basis functions (used in resolution of the identity fitting) are given by χ_Q and fragments are indicated as I, J or F_I, F_J .

Fragment-localized quantities will be made explicit through the use of connecting lines above or below: for instance, two MOs p and q are constrained to a single fragment, F_I , if their indexes are connected as \overline{pq} or \underline{pq} . Throughout the discussion of the algorithms, when discussing the scaling, capital letters will denote quantities that scale with the size of the system (e.g. O for all occupied orbitals) and lower case letters indicate that the value is dependent only on the identity of a given fragment (e.g. n for basis functions on a single fragment). In particular, in our analysis of homogeneous atomic or molecular clusters, we shall consider them to contain M identical fragments; thus, the computational effort can be evaluated as a power of M . Finally, the notation

(MM) will be used to indicate quadratic scaling for small systems and linear scaling for sufficiently large systems.

2.2. Ground-State Wave Function with Absolutely Localized Molecular Orbitals. The ground-state Hartree–Fock wave function is a Slater determinant of one-electron functions:

$$|\Psi_0\rangle = |\psi_1 \dots \psi_i \psi_j \dots \psi_n\rangle \quad (2)$$

For standard electronic structure calculations, the ψ_i terms are canonical MOs, which diagonalize the Fock operator and are typically highly delocalized. The MOs are expanded, in terms of atom-centered basis functions (AOs), as

$$|\psi_p\rangle = \sum_\mu |\chi_\mu\rangle c_{\mu p}^\mu \quad (3)$$

where the AOs (χ_μ) are assumed to be contracted Gaussians.

The atom-centered AOs used in electronic structure theory calculations are naturally partitioned according to the fragment on which they reside. ALMOs arise by applying the constraint that the MO coefficient matrix should be fragment-blocked, such that the ALMOs that describe an atom or molecule in a cluster contain only contributions from the AOs of that specific fragment.⁶⁰ When using ALMOs, each molecular orbital is tagged to a fragment F_I and expanded only in the subset of basis set functions that centers on with fragment.

$$|\psi_p\rangle = \sum_{\mu \in F_I} |\chi_\mu\rangle c_{\mu p}^\mu \quad p \in F_I \quad (4)$$

The resulting ALMOs are nonorthogonal between fragments, although the ALMOs on a single fragment can be chosen to be orthogonal. The block-diagonal structure of the ALMO transformation leads to very high computational efficiency. It is highly desirable to maintain this local structure for excited state evaluation, as will be discussed further in Section 3.3.

In tensor notation, the overlap of nonorthogonal orbitals, such as the ALMOs, is defined by the covariant overlap metric,

$$\langle \psi_p | \psi_q \rangle = \sigma_{pq} = S_{pq} \quad (5)$$

and, similarly, the contravariant metric is

$$\langle \psi^p | \psi^q \rangle = \sigma^{pq} = \sigma_{pq}^{-1} = S_{pq}^{-1} \quad (6)$$

The biorthogonality of the covariant and contravariant subspaces implies

$$\langle \psi^p | \psi_q \rangle = \delta_{\overline{pq}} \quad (7)$$

The nonorthogonality of ALMOs between fragments has the interesting implication that the so-called “virtual” ALMOs, $|\psi_a\rangle$, are not strictly virtual, because they overlap occupied ALMOs on other fragments: $\langle \psi_k | \psi_a \rangle \neq 0$ for $k \in F_I$ and $a \in F_J$. To obtain well-defined virtual functions, it is necessary to remove contamination in $|\psi_a\rangle$ from the occupied subspace. Projecting the occupied ALMOs $|\psi_k\rangle$ from the virtual ALMOs $|\psi_a\rangle$ yields new (projected) virtuals $|\phi_a\rangle$. The $|\phi_a\rangle$ terms are orthogonal to all occupied ALMOs by construction, but remain nonorthogonal among themselves.

$$\begin{aligned} |\phi_a\rangle &= \mathcal{N}_a (|\psi_a\rangle - \hat{P}_{\text{occ}} |\psi_a\rangle) = \mathcal{N}_a (|\psi_a\rangle - |\psi_k\rangle \sigma^{kl} \langle \psi_l | \psi_a \rangle) \\ &= \mathcal{N}_a (|\psi_a\rangle - |\psi_k\rangle \sigma^{kl} \sigma_{la}) = \mathcal{N}_a (|\psi_a\rangle - |\psi_k\rangle d_{\overline{ka}}^k) \end{aligned} \quad (8)$$

Here, \mathcal{N}_a is a normalization factor to ensure $\langle \phi_a | \phi_a \rangle = 1$, and $d_{\overline{ka}}^k = \sigma^{kl} \sigma_{la}$.

2.3. Nonorthogonal CIS and the ALMO–CIS Model.

Singly substituted configurations are formed by promoting an electron from an occupied orbital to a virtual orbital that is orthogonal to the occupied one. Note these are the projected orbitals so that they are properly orthogonal to the occupied space.

$$|\Psi_{\cdot a}^i\rangle = |\psi_1 \dots \phi_a \psi_j \dots \psi_n\rangle \quad (9)$$

The CIS excited states are superpositions of all single substitutions, with amplitudes of $t_{\cdot i}^a$:

$$|\Psi_{\text{CIS}}\rangle = a_a^\dagger a_i |\Psi_0\rangle t_{\cdot i}^a = |\Psi_{\cdot a}^i\rangle t_{\cdot i}^a \quad (10)$$

Substituting this wave function into the time-independent Schrödinger equation and projecting with each of the excited determinants according to the linear variational principle yields equations for the CIS excitation energies.

$$\langle \Psi_{\cdot j}^b | \hat{H} | \Psi_{\cdot a}^i \rangle t_{\cdot i}^a = E_{\text{CIS}} \langle \Psi_{\cdot j}^b | \Psi_{\cdot a}^i \rangle t_{\cdot i}^a \quad (11)$$

The choice of the natural representation⁶⁹ makes evaluation of the matrix elements isomorphic to the conventional orthonormal case, because biorthogonality of covariant and contravariant functions permits similar simplifications. Recalling eq 7, we see that

$$\langle \Psi_{\cdot j}^b | \Psi_{\cdot a}^i \rangle = \delta_{\cdot j}^i \delta_{\cdot a}^b \quad (12)$$

Carefully evaluating the matrix elements leads to the following eigenvalue equation in the natural representation (this is a generalized version of the conventional result, where biorthogonality replaces orthogonality):

$$A_{\cdot j a}^{i b} t_{\cdot i}^a = \omega_{\text{CIS}} \delta_{\cdot a}^b \delta_{\cdot j}^i t_{\cdot i}^a \quad (13)$$

where $\omega_{\text{CIS}} = E_{\text{CIS}} - E_0$.

The matrix elements of the singles–singles block of the Hamiltonian are given in the biorthogonal representation as

$$A_{\cdot j a}^{i b} = f_{\cdot a}^b \delta_{\cdot j}^i - f_{\cdot j}^i \delta_{\cdot a}^b + \langle \psi^i \phi^b | \phi_a \psi_j \rangle \quad (14)$$

These equations can be transformed to the covariant integral representation (where the unknown amplitudes are fully contravariant, while the known matrix elements are fully covariant)

$$A_{i b j a} t^{a i} = \omega_{\text{CIS}} S_{a b} S_{i j} t^{a i} \quad (15)$$

$$A_{i b j a} = f_{b a} S_{i j} - f_{i j} S_{b a} + \langle \psi_i \phi_b | \phi_a \psi_j \rangle \quad (16)$$

Introducing the overlap matrix here and transforming to the natural representation preserves the Hermiticity of the Hamiltonian and the variational nature of the wave function.

For closed-shell singlet wave functions, the spin-restricted form, with all dimensions collapsed to those of spatial orbitals rather than spin orbitals, is

$$A_{i b j a} = f_{b a} S_{i j} - f_{i j} S_{b a} + 2(\psi_i \phi_a | \phi_b \psi_j) - (\psi_i \psi_j | \phi_b \phi_a) \quad (17)$$

The spatial orbital two-electron integrals are written in the “chemist’s notation”, where the first two indexes involve the coordinates of electron 1 and the last two indexes are those of electron 2.

The nonorthogonal CIS equations, as written, convey computational advantage only when the one- and two-electron matrix elements become sufficiently sparse that the dimension of the problem can be greatly reduced. As argued in the [Introduction](#), this is very difficult to exploit computationally except for truly enormous systems. For clusters on the order of 1000 atoms, there is very little effective sparsity, because of the spatially extended

basis sets that are needed to treat Rydberg excited states (equivalent to at least doubly augmented basis sets, in terms of the Dunning hierarchy or the (2+) sets, in terms of diffuse functions for Pople basis sets).

Instead, we build a physically based model, akin to local correlation models, which restricts the single substitutions to only occur within fragments. This prohibits charge transfer between fragments. In the limit of noninteracting fragments, such a model is exact. As discussed in the [Introduction](#), it is also likely to be quite accurate for weakly interacting clusters if their constituent atoms or molecules have high ionization potentials and low (or negative) electron affinities.

We shall refer to this model where the excited states are approximated as superpositions of intrafragment single substitutions as “ALMO–CIS”. Considering homogeneous atomic or molecular clusters containing M fragments, it is evident that the ALMO–CIS model retains only $O(M)$ of the original $O(M^2)$ CIS amplitudes. The model includes locality at the design level, and it will also be relatively easy to exploit this. The ALMO–CIS equations follow from the nonorthogonal CIS equations in the covariant integral representation by deleting all rows and columns corresponding to single substitutions that transfer charge between fragments:

$$\mathcal{A}_{i a, j b} t^{a i} = \omega_{\text{CIS}} \mathcal{S}_{i a, j b} t^{a i} \quad (18)$$

with

$$\mathcal{A}_{i a, j b} = A_{i b j a} \text{ and } \mathcal{S}_{i a, j b} = S_{i j} S_{a b}. \quad (19)$$

2.4. ALMO–CIS Oscillator Strengths. The oscillator strength for an electronically excited state κ reflects the probability of a transition from the ground state into that state and is generally defined (in atomic units):

$$f_{\kappa} = \frac{2}{3} (E_{\kappa} - E_0) |\langle \Psi_0 | \hat{\mu} | \Psi_{\kappa} \rangle|^2 \quad (20)$$

The energy difference comes directly from the calculation of the ALMO–CIS eigenvalues, and the dipole expectation value is given from the projected ALMOs as

$$\langle \Psi_0 | \hat{\mu} | \Psi_{\kappa} \rangle = \sum_{F, J} \sum_{i, a \in \{\Psi_J\}} t_{\kappa}^{a i} \langle \psi_i | \hat{\mu} | \phi_a \rangle. \quad (21)$$

The dipole matrix elements can then readily be determined from the available AO basis matrix elements.

$$\langle \psi_i | \hat{\mu} | \phi_a \rangle = (\psi_i | \chi^{\mu}) (\chi_{\mu} | \hat{\mu} | \chi_{\nu}) (\chi_{\nu} | \phi_a) = c_{\cdot i}^{\mu \dagger} \mu_{\mu \nu} c_{\cdot a}^{\nu}. \quad (22)$$

3. EFFICIENT IMPLEMENTATION AND SCALING

An efficient implementation of the ALMO–CIS method has been completed within the Q-CHEM electronic structure program.^{71,72} The following subsections describe the key design aspects of the algorithm that we have developed and implemented.

3.1. Direct Versus Iterative Diagonalization. The first key design decision is how the truncated Hamiltonian should be diagonalized: directly, by dense linear algebra, or iteratively, using matrix-vector multiplication.⁷³ While iterative diagonalization is greatly preferred if only a few eigenvalues are desired, direct diagonalization is more efficient if a significant fraction of the eigenvalues are sought. Our first target application of ALMO–CIS is to compute the excited states of large homogeneous clusters. These typically have many excited states within a narrow energy window, corresponding to bands that broaden

the discrete excitations of the spectrum of a single fragment; thus, a large percentage of the CIS eigenvalues is desired.

Therefore, we choose direct diagonalization as the basis of this implementation. We note that this is not a serious limitation on the size of system that can be treated via ALMO–CIS, as the ALMO–CIS vectors are $O(M)$ and thus construction of the ALMO–CIS Hamiltonian requires $O(M^2)$ storage, and direct diagonalization is $O(M^3)$ for the full spectrum. By contrast, conventional CIS involves eigenvectors of length $O(M^2)$ and therefore requires $O(M^4)$ storage and $O(M^6)$ computational effort for direct diagonalization. The ALMO–CIS calculation involves storage and computation that is proportional to only the square root of that for conventional CIS. Or, for equivalent computational resources, ALMO–CIS will be able to treat a system of $O(M^2)$ size if conventional CIS can treat a system of size $O(M)$.

3.2. Strategy for Two-Electron Integral Evaluation.

Generally, the most computationally demanding step in standard CIS is associated with the formation and transformation of the two-electron repulsion integrals (ERIs). There are two basic issues that dictate our strategy. First is the extent to which basis function overlaps become sparse in a large cluster. Second is the question of the likely effectiveness of the resolution of the identity (or density fitting) approach. We shall discuss these issues separately, and then outline our chosen approach.

With regard to the first issue, AO-ERI calculations naïvely scale as $O(M^4)$. In large molecules with compact basis sets, this can be reduced to quadratic cost by applying appropriate screening techniques, such as the Schwarz integrals, which yield a strict upper bound to the size of the integrals.^{74,75}

$$|(\mu\nu|\lambda\sigma)| \leq (\mu\nu|\mu\nu)^{1/2}(\lambda\sigma|\lambda\sigma)^{1/2} \quad (23)$$

The number of significant basis function pairs, with a threshold of $1 \times 10^{-12} E_h$ are shown in Figure 1 as a function of cluster size for

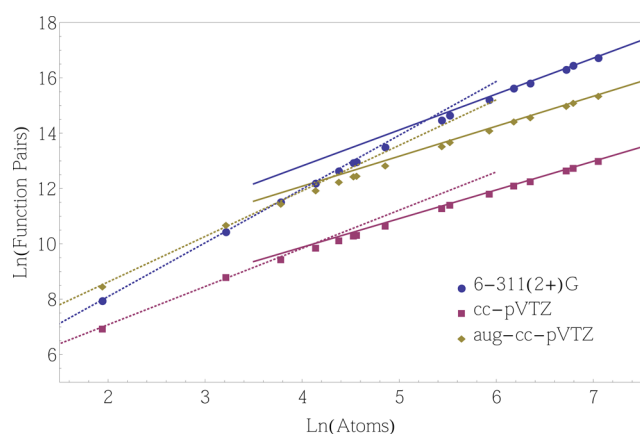


Figure 1. Scaling of the significant basis function pairs with system size (He_7 to He_{1159}). A linear fit to the last five points on each curve gives slopes of 1.3 for the custom 6-311(2+)G basis set (11 functions/atom), 1.0 for the standard aug-cc-pVTZ basis set (23 functions/atom), and 1.1 for the cc-pVTZ basis set (14 functions/atom). The dashed lines are fits to the first three points to illustrate the onset of basis function sparsity.

regularly spaced helium clusters using the cc-pVTZ basis, aug-cc-pVTZ, and a customized [5s2p] basis (consisting of the 3 s functions of 6-311G and two sets of diffuse s and diffuse p exponents, subsequently denoted 6-311(2+)G) that is suitable for describing

the $n = 2$ Ry manifold.⁵⁸ It is evident that effective linear scaling is not obtained with the diffuse basis set until clusters of well over 1000 atoms as the slope is still larger than 1, even at He_{1159} . By contrast, the compact cc-pVTZ basis reaches linear scaling in its number of numerically significant basis function pairs much sooner (at ~ 60 atoms). Therefore, excited-state calculations, which are dependent on diffuse basis functions, face growth in the number of significant AO-ERIs that remain close to $O(M^4)$ into regimes as large as 1000 atoms. As a result, evaluation of the MO-ERIs by naïve transformation of AO-ERIs would be at least this demanding, and therefore will not be computationally efficient.

However, the ALMO–CIS model offers crucial additional computational advantages. The ALMO occupied orbitals and the unprojected virtual orbitals are both fragment-blocked; as a result, if we ignore the projection terms, the ALMO–CIS model rigorously requires only $O(M^2)$ AO-ERIs. Let us begin by expanding the Coulomb-like term, $(\psi_i\phi_a|\psi_j\phi_b)$, of eq 17, in terms of unprojected ALMO contributions and projection corrections:

$$\begin{aligned} (\psi_i\phi_a|\psi_j\phi_b) &= \mathcal{N}_a\mathcal{N}_b \left\{ (\psi_i\psi_a|\psi_j\psi_b) \right. \\ &\quad \left. - 2(\psi_i\psi_a|\psi_j\psi_k)(\psi^k|\psi_b) + (\psi_i\psi_k|\psi_j\psi_l)(\psi^k|\psi_a)(\psi^l|\psi_b) \right\} \\ J &= N^2(J1 - 2 \cdot J23 + J4) \end{aligned} \quad (24)$$

Because of the fragment blocking of the ALMO MO coefficient matrix, the AO-ERIs necessary to evaluate the unprojected contribution, $(\psi_i\psi_a|\psi_j\psi_b)$ (i.e., J1), will be just the $(\chi_\mu\chi_\nu|\chi_\lambda\chi_\sigma)$ subset.

Similarly, the exchange term, $(\psi_i\psi_j|\phi_a\phi_b)$, of eq 17 can be written as

$$\begin{aligned} (\psi_i\psi_j|\phi_a\phi_b) &= \mathcal{N}_a\mathcal{N}_b \left\{ (\psi_i\psi_j|\psi_a\psi_b) \right. \\ &\quad \left. - 2(\psi_i\psi_j|\psi_a\psi_k)(\psi^k|\psi_b) + (\psi_i\psi_k|\psi_j\psi_l)(\psi^k|\psi_a)(\psi^l|\psi_b) \right\} \\ K &= N^2(K1 - 2 \cdot K23 + K4) \end{aligned} \quad (25)$$

Here, the $(\chi_\mu\chi_\nu|\chi_\lambda\chi_\sigma)$ AO-ERIs are needed for the unprojected ALMO contributions $((\psi_i\psi_a|\psi_j\psi_b)$ or K1). This is true even if all $O(M^4)$ AO-ERIs are nonzero.

These results suggest that we should evaluate the *unprojected* contributions to the ALMO–CIS Coulomb and exchange integrals by fragment-blocked transformation of the $O(M^2)$ required AO-ERIs, and then compute the corrections separately. Therefore, the unprojected ALMO–CIS integrals will require only $O(M^2)$ computational effort. The corrections for projection require evaluating ALMO integrals with three occupied indexes, $(\psi_i\psi_a|\psi_j\psi_k)$, $(\psi_i\psi_j|\psi_a\psi_k)$, and four occupied indexes, $(\psi_i\psi_k|\psi_j\psi_l)$. These corrections are significantly smaller in magnitude and can be evaluated using the resolution of the identity (RI) approximation without significant loss of accuracy.^{76,77} Doing these corrections via RI avoids the need for larger numbers of four-center AO-ERIs and permits the efficiency of dense linear algebra.

3.3. ALMO Integral Evaluation. The half-transformed integrals $J_{\mu\nu}^{ia} = (\psi_i\psi_a|\chi_\mu\chi_\nu)$ and $K_{\mu\nu}^{ia} = (\psi_i\chi_\mu|\psi_a\chi_\nu)$ are computed within Q-CHEM's AO-ERI evaluation code, which uses the PRISM algorithm for efficiency.^{78–80} We have added a customized ERI “digestor” that carries out the first two MO quarter-transformations on a batch of AO-ERIs. The batch size is determined by the integral code and does not scale with the size of the system. The fully transformed integrals are then formed from the half-transformed integrals externally.

Algorithm 1: Coulomb digestor for integrals, $J_{ia\lambda\sigma} = (\psi_i\psi_a | \chi_\lambda\chi_\sigma)$

```

for  $\mu\nu \in F_I$  do
  for  $\lambda\sigma$  batches do
    Make  $(\mu\nu | \lambda\sigma)$  for  $\mu\nu, \lambda\sigma$ 
    for  $\lambda\sigma \in batch$  do
       $F_J \leftarrow \lambda\sigma$ 
       $J_{ia\lambda\sigma} += (\mu\nu | \lambda\sigma) P_{ia}^{\mu\nu}, \forall \bar{ia} \in F_I$ 
       $J_{jb\mu\nu} += (\mu\nu | \lambda\sigma) P_{jb}^{\lambda\sigma}, \forall \bar{jb} \in F_J$ 

```

Algorithm 2: Exchange integrals, $K_{iav\lambda} = (\psi_i\chi_\nu | \psi_a\chi_\lambda)$

```

for  $\mu\nu$  do
  for  $\lambda\sigma$  exchange batches do
     $F_I \leftarrow \lambda, F_J \leftarrow \sigma$ 
    Make  $(\mu\nu | \lambda\sigma)$  for  $\mu\lambda \in F_I, \nu\sigma \in F_J$ 
    for  $\lambda\sigma \in batch$  do
       $K_{jb\mu\lambda} += (\mu\nu | \lambda\sigma) P_{jb}^{\nu\sigma}, \forall \bar{jb} \in F_J$ 
       $K_{jb\lambda\mu} += (\mu\nu | \lambda\sigma) P_{jb}^{\sigma\nu}, \forall \bar{jb} \in F_J$ 
       $K_{ia\nu\sigma} += (\mu\nu | \lambda\sigma) P_{ia}^{\mu\lambda}, \forall \bar{ia} \in F_I$ 
       $K_{ia\sigma\nu} += (\mu\nu | \lambda\sigma) P_{ia}^{\lambda\mu}, \forall \bar{ia} \in F_I$ 
    if  $F_I == F_J$  then
      for  $\lambda\sigma \in batch, \bar{ia} \in F_I$  do
         $K_{ia\mu\sigma} += (\mu\nu | \lambda\sigma) P_{ia}^{\bar{\lambda}}$ 
         $K_{ia\sigma\mu} += (\mu\nu | \lambda\sigma) P_{ia}^{\bar{\nu}}$ 
         $K_{ia\nu\lambda} += (\mu\nu | \lambda\sigma) P_{ia}^{\mu\sigma}$ 
         $K_{ia\lambda\nu} += (\mu\nu | \lambda\sigma) P_{ia}^{\sigma\mu}$ 

```

Only the integrals with ψ_i and ψ_a on F_p and χ_μ and χ_ν on F_j are required (corresponding to $(\chi_\mu\chi_\nu | \chi_\lambda\chi_\sigma)$ and $(\chi_\mu\chi_\nu | \chi_\lambda\chi_\sigma)$, as discussed in the previous subsection). No additional truncation is possible within the coulomb integrals, but for the exchange contributions, using the Schwarz integrals, only AO-ERIs with significant overlap need be computed. By creating mini-lists of the required half-transformed integrals, we avoid forming many of the AO integrals.^{24,81}

The AO integrals are efficiently transformed using customized digestor algorithms. The coulomb digestor is outlined in Algorithm 1, and the exchange digestor is shown in Algorithm 2. These algorithms are shown schematically rather than exactly as implemented in order to avoid undue complexity. In particular, the production code is organized into loops over different angular momentum classes for bras and kets, and then loops over the different shell quartets corresponding to the current bra and ket angular momentum. Finally batches of selected shell quartets are evaluated. By contrast, the simplified schematics shown in Algorithms 1 and 2 show only loops over AO function pairs.

For the coulomb integrals, a batch of AO integrals are contracted with the transition densities $P_{ia}^{\mu\nu} = c_i^\mu c_a^{\nu\dagger}$. Each integral batch corresponds to a single bra, $\langle \chi_\mu\chi_\nu |$, so each of its members can be identified with a specific ket, $|\chi_\lambda\chi_\sigma\rangle$. Here, λ and σ must belong to the same fragment F_j . The digestor loops over the elements of the batch and identifies the corresponding fragment F_j . This is followed by gathering the relevant elements of the density matrix for the ket side belonging to F_j , $P_{jb}^{\lambda\sigma}$. Note that the density matrix is symmetrized and vectorized by fragment, to further increase the efficiency. Multiplication of the AO integrals and the density matrix is performed, while accounting for the symmetry of the half-transformed integrals $J_{\mu\nu\bar{jb}}$ are incremented.

The digestor for the coulomb-like terms uses a symmetrized transition density and yields a half-transformed matrix that is also symmetrized. By contrast, the exchange terms (Algorithm 2) cannot accept a symmetrized density and result in an unsymmetric half-transformed tensor. Thus, all symmetries must be explicitly

taken into account. It is also important to emphasize, in addition to computational costs, which only grow as $O(M^2)$, even when there are as many as $O(M^4)$ significant AO-ERIs, these routines are also designed to ensure, at the most, $O(M^2)$ storage requirements. Both the input transition densities and the output half-transformed matrices are stored in packed format, keeping only the required values. Finally, while not shown explicitly, the final two quarter transformations are also done by making use of the ALMO locality and scale no higher than $O(M^2)$.

3.4. ALMO Integral Corrections. The smaller terms, which are still critical for accurate evaluation of the two-electron integrals from eqs 24 and 25 include J_{23} , J_4 , K_{23} , and K_4 . These will be evaluated using the RI approximation, following algorithms described below.

For compactness, the three-center density-fit integrals will be denoted as $v_{ijP} = (\psi_i \psi_j | \chi_P)$ and $v_{iaP} = (\psi_i \psi_a | \chi_P)$. Similarly, the two-center ERIs in the auxiliary basis will be denoted as $v_{PQ} = (\chi_P | \chi_Q)$, while elements of its inverse will be written as v^{PQ} . In this notation, the RI correction terms, first introduced in eqs 24 and 25, can be explicitly written as follows:

$$J_{23} = v_{iaP} v^{PQ} v_{ijkQ} \sigma_b^k \quad (26)$$

$$J_4 = \sigma_a^k v_{ikP} v^{PQ} v_{ijlQ} \sigma_b^l \quad (27)$$

$$K_{23} = v_{ijP} v^{PQ} v_{akQ} \sigma_b^k \quad (28)$$

$$K_4 = v_{ijP} v^{PQ} v_{klQ} \sigma_a^k \sigma_b^l \quad (29)$$

There are two primary steps to determine these correction terms. First, the RI integrals must be generated, and then they are combined to form the final corrections. The RI integrals in the AO basis are formed in batches and subsequently transformed using a customized digester within the AOints module of Q-CHEM, shown in Algorithm 3. Two types of integrals are

Algorithm 3: 3-center integrals v_{ijP} , v_{iaP}

```

for batch = 1,  $N_{\text{bat}}$  do
  for  $\mu\nu = 1, (NN)$  do
    calculate  $(\mu\nu | P)$ 
    determine  $F_I$  from current  $\mu$ 
    for  $i \in F_I, (i|\nu) > \text{thresh}$  do
      for  $P \in \text{batch}$  do
         $(i\nu | P) += (\mu\nu | P) \cdot c_i^\mu$ 
    for  $i = 1, O$  do
      for  $j\nu = 1, On, (i|j) > \text{thresh}$  do
        for  $P \in \text{batch}$  do
           $(ij | P) += (i\nu | P) \cdot c_j^\nu$ 
        write  $(ij | P)$  to disk: current  $i, P \in \text{batch}, \forall j(\text{significant})$ 
    for  $i = 1, O$  do
      for  $a\nu = 1, Vn$  do
        for  $P \in \text{batch}$  do
           $(ia | P) += (i\nu | P) \cdot c_a^\nu$ 
        write  $(ia | P)$  to disk: current  $i, P \in \text{batch}, \forall a$ 

```

needed: those with both indices occupied (v_{ijP}) and those with one occupied and one virtual (v_{iaP}). The number of occupied–occupied integrals that are required will grow linearly, with respect to system size in large enough systems, since ψ_i and ψ_j are both highly localized on their respective fragments and do not have a large spatial extent. The number of pairs of occupied–virtual integrals will be much larger, because the virtual orbitals are significantly more diffuse; however, they are still ALMOs and retain the associated advantages in efficiency. Using our efficient

implementation, the cost to form the transformed three-center ERIs does not exceed $O(M^3)$ with system size. By computing only the significant occupied–occupied RI integrals, the final combination of the integrals to form the correction terms can also be made to scale as $O(M^3)$ with system size or lower.

In generating the three-center AO integrals, the auxiliary basis consisting of N_{aux} functions is partitioned into N_{bat} batches based on shell structure to avoid memory issues. Because of this batching policy, the three-center integrals are formed in the “shell” order (i.e., sorted by angular momentum) of the auxiliary basis. Conventionally, when writing to disk, the digested (ALMO-transformed) integrals are transformed back into their “natural order” (i.e., sorted by atoms). The low efficiency of this seek-dominated input/output (I/O) procedure eventually makes this the rate-determining step of the ALMO–CIS calculation for large systems. The two-center integrals v_{PQ} are formed in the same order to ensure consistency of auxiliary basis ordering, after minimal modification to the existing code. After looping over batches, there is a loop over the significant basis function pairs, which is quadratic for small systems and linear for sufficiently large clusters. Subsequent loops in the first block of Algorithm 3 depend only on the identity of the fragments and do not grow with the system size. The final two blocks shown here transform the AO 3-center integrals to ALMO 3-center integrals.

The initial steps for assembling the RI correction terms are common to both the coulomb and exchange terms and are shown in Algorithm 4. Algorithm 5 then shows the steps for computing the coulomb corrections. For transparency of computational cost, all multiplications are written as loops. Those that grow in cost linearly with the size of the system are shown in purple font, whereas loops shown in blue font are over sparse indices that scale quadratically for small systems but linearly for large systems. The exchange corrections are computed similarly (Algorithm 6). These transformations will grow asymptotically as $O(M^3)$, which is the same scaling as for the matrix diagonalization. However, for small systems, they will scale quartically, because the full benefits from using ALMOs do not appear immediately.

4. RESULTS

We employ helium clusters as test systems to explore the accuracy and computational cost of the ALMO–CIS method. We then use our method to examine the size dependence of electronic spectrum associated with the $n = 2$ levels. As discussed in the Introduction, helium clusters are likely suitable for the ALMO–CIS method, because the high ionization potential and negative electron affinity make the discarded charge-transfer (CT) configurations high in energy, relative to the retained atomic excitations. Therefore, we expect CT effects to be secondary. Tests exploring this question are reported in section 4.1 by comparing ALMO–CIS to standard CIS for medium-sized He_{25} clusters. In section 4.2, a detailed analysis of the computational performance of the code is reported, spanning clusters from 7 atoms to 485 atoms. With these characterizations in hand, in section 4.3, we turn to a pilot application of the ALMO–CIS method, on the size dependence of the excitation spectrum.

4.1. Accuracy. To determine the accuracy of ALMO–CIS, it was first applied to small 25-atom clusters, which have previously been studied in depth using CIS.^{58,59} For the $n = 2$ manifold, 100 states are required to fully characterize the band, with the lowest 25 states characterized primarily by super-

Algorithm 4: RI Corrections

```

for  $ij = 1, (OO)$  do
  for  $P = 1, N_{aux}$  do
    for  $Q = 1, N_{aux}$  do
       $c_{ij}^P += v^{PQ} \cdot v_{ijQ}$ 

for  $ij = 1, (OO)$  do
  for  $kl = 1, (OO)$  do
    for  $P = 1, N_{aux}$  do
       $\mathcal{V}_{ijkl} += c_{ij}^P \cdot v_{klP}$ 

for  $ia = 1, Ov$  do
  for  $jk = 1, (OO)$  do
    for  $P = 1, N_{aux}$  do
       $\mathcal{V}_{iajk} += c_{jk}^P \cdot v_{iaP}$ 

for  $ia = 1, Ov$  do
  for  $jk = 1, (OO)$  do
    if  $(i | j) > \text{thresh}$  then
      for  $P = 1, N_{aux}$  do
         $\mathcal{V}_{iak} += c_{ij}^P \cdot v_{akP}$ 

```

Algorithm 5: Coulomb RI Corrections

```

for  $ia = 1, Ov$  do
  for  $jl = 1, (OO)$  do
    for  $k = 1, O$  do
      if  $(k | i) > \text{thresh}$  then
         $\mathcal{W}_{iajl} += \mathcal{V}_{ikjl} \cdot \sigma_a^k$ 

for  $jb = 1, Ov$  do
  for  $l = 1, O$  do
    if  $(j | l) > \text{thresh}$  then
       $J23_{iajb} += \mathcal{V}_{iajl} \cdot \sigma_b^l$ 
       $J4_{iajb} += \mathcal{W}_{iajl} \cdot \sigma_b^l$ 

```

Algorithm 6: Exchange RI Corrections

```

for  $ia = 1, Ov$  do
  for  $j = 1, O$  do
    if  $(i | j) > \text{thresh}$  then
      for  $kl = 1, (OO)$  do
         $\mathcal{W}_{ijal} += \mathcal{V}_{ijkl} \cdot \sigma_a^k$ 

for  $jb = 1, Ov$  do
  for  $l = 1, O$  do
     $K23_{ijab} += \mathcal{V}_{ijal} \cdot \sigma_b^l$ 
     $K4_{ijab} += \mathcal{W}_{ijal} \cdot \sigma_b^l$ 

```

positions of 2s-type orbitals and the remaining 75 states characterized as 2p-type. Figure 2 shows a first comparison of the excitation spectrum calculated with full CIS against the simplified ALMO–CIS model, at a single local minimum of He₂₅. It is evident that the general form of the density of states is entirely preserved by ALMO–CIS: a clear distinction remains between the 25 states of 2s character, and the 75 states of 2p character. This is an encouraging validation of the ALMO–CIS model.

The low-energy part of the 2s and 2p state manifolds is systematically more accurately reproduced by ALMO–CIS than the high-energy part. The error is entirely due to charge transfer. It is quite logical that the higher energy states in the manifold will have greater error due to neglect of CT, because the

discarded ionic configurations gradually become separated by smaller energy differences from the state of interest. It is also reasonable that errors in the 2p manifold are larger than those in the 2s manifold, simply because this is a higher-energy window, and therefore CT corrections can contribute more to energy stabilization.

These conclusions transfer to other nuclear configurations. As can be seen in Figure 3 for five sample configurations of the He₂₅ cluster, the ALMO–CIS errors, measured against CIS, are qualitatively consistent from geometry to geometry. They begin very small at the red end of both the s and p manifolds and increase with increasing state number. The maximum error is 0.4–0.5 eV (<2.5%), which is non-negligible, but less than the standard CIS error of ~1 eV. For application

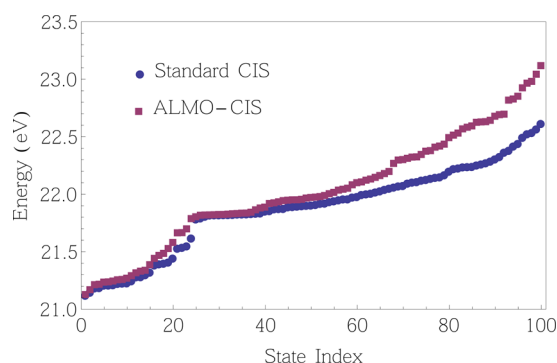


Figure 2. Excitation energy for a single geometry of He_{25} as a function of increasing state, evaluated by CIS and ALMO-CIS, for 100 states in the $n = 2$ manifold. A modified 6-311(2+)G basis with 11 functions per He atom was employed.⁵⁸ He_{25} states 1–25 are predominantly of $2s$ character and states 26–100 are predominantly of $2p$ character. The error increases monotonically and smoothly within a band.

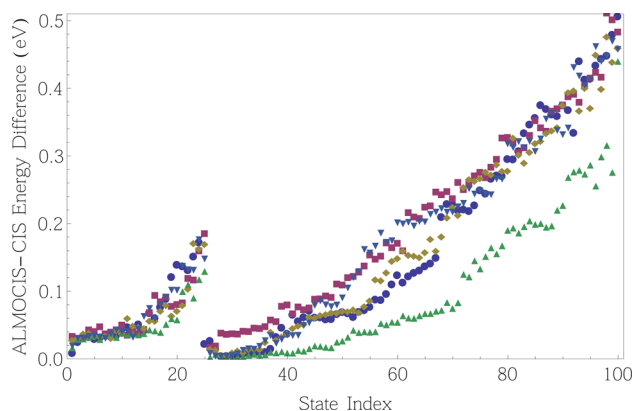


Figure 3. $E_{(\text{ALMO-CIS})} - E_{(\text{CIS})}$: This plot shows the excitation energy differences (eV) between ALMO-CIS and CIS, as a function of state for five different He_{25} ground-state geometries (i.e., local minima). He_{25} states 1–25 are s -like and states 26–100 are p -like. ALMO-CIS is almost identical to CIS for the lowest energy $2s$ and $2p$ states. The maximum errors occurs for the states at the blue end of the excited $2p$ manifold.

purposes the important point is that the errors all have the same sign, and increase gently and systematically from state to state. This suggests that a qualitatively correct spectrum will be obtained, with the highest accuracy at the red edge, and exaggerated width of the blue tail of particularly the $2p$ manifold. The ALMO-CIS spectrum can ultimately be corrected by appropriate scaling.

The spectrum for He_{25} at the CIS/6-311(2+)G level of theory was previously computed⁵⁸ using 100 randomized clusters with geometries optimized using Møller–Plesset perturbation theory (MP2/6-311G). Since $1s \rightarrow 2s$ transitions are symmetry-forbidden, the s states of the cluster only contribute weakly to the optical spectrum, which is dominated by a broad peak corresponding to the p states. This peak has the atomic excitation energy as its lower bound, and spreads over a range of ~ 2 eV. Using these same structures for the ALMO-CIS/6-311(2+)G spectrum, we obtain the results shown in Figure 4, which are compared to the corresponding CIS spectrum.

Qualitatively, the results shown in Figure 4 are exactly as anticipated based on inspecting the CIS and ALMO-CIS excitation energies for a single configuration in Figure 2, or the

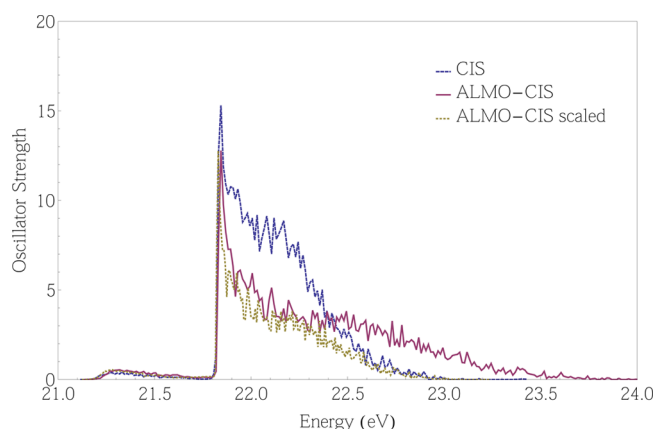


Figure 4. Absorption spectra calculated for a He_{25} cluster at the CIS (solid blue) and ALMO-CIS (solid pink) level of theory. The dashed gold curve shows the ALMO-CIS spectrum, where the energies have been corrected by the systematic error.

ALMO-CIS errors for five different configurations shown in Figure 3. In the lowest excited states of the 25-atom clusters (at the red end of the spectrum), very little error is introduced by the ALMO-CIS approximation. As discussed previously, the blue tail of the ALMO-CIS spectrum is extended to higher energies, relative to the CIS spectrum. Interestingly, there is a second effect, which is that we see a loss of integrated oscillator strength in the $2p$ band calculated by ALMO-CIS, relative to CIS. It may be directly inferred that the neglected CT configurations do contribute non-negligibly to oscillator strength, even in the low-energy part of the $2p$ band, where they contribute very little to the excitation energy. However, the relative intensities throughout the band are generally preserved, which justifies qualitative comparisons.

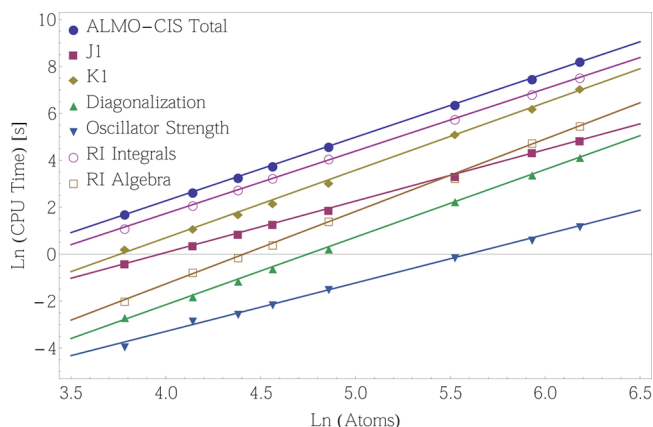
Further physical insight into the origin of the deviations can be obtained from the detailed analysis of the CIS spectrum reported previously.⁵⁸ States at the higher-energy edge of the spectrum tend to result from excitations of atoms in the center of the cluster, while the low-energy edge (near the atomic excitation energy) correspond to atoms at the surface. The extended $2s$ and $2p$ Rydberg orbitals of a bulk atom overlap the ground-state $1s$ orbital of their neighbors, destabilizing the cluster by Pauli repulsion. It is reasonable to expect states dominated by these bulk contributions to be most affected by CT, because they better overlap with those from other atoms to yield more significant matrix elements for CT.

4.2. Timings. The main advantage of the ALMO-CIS method is that it theoretically has a very low computational cost: $O(M^3)$ as a function of cluster size for the full eigenspectrum. This contrasts with the $O(M^6)$ computational effort associated with obtaining all eigenstates with standard CIS. As discussed in section 3.1, the diagonalization step is straightforwardly third order in system size. However, significant effort is required to formulate an efficient algorithm for the evaluation of the matrix elements to realize $O(M^3)$ scaling in practice. The timings reported here result from calculations using a single core on an AMD Opteron 6300 series using helium clusters ranging from He_{44} to He_{485} with regularly spaced atoms (4 Å), using the same customized 6-311(2+)G basis as the previous subsections.

Overall, the method scales as desired (see Table 1), revealing overall growth of computational effort just below $O(M^3)$ in the size range from He_{44} to He_{485} . The relative magnitude of the

Table 1. Theoretical and Actual Scaling for Total ALMO–CIS Calculation and Diagonalization

component	Scaling	
	predicted	observed
diagonalization	M^3	2.88
total	M^3	2.71

**Figure 5.** CPU timing data for ALMO–CIS. The clusters in this plot range from 44 atoms to 485 atoms. The slope of the line corresponding to the total ALMO–CIS time is 2.71, indicating that the scaling is overall $O(M^3)$ in computational effort, as a function of the number of atoms (M).

ALMO–CIS components can be seen in Figure 5. Although, matrix diagonalization is strictly $O(M^3)$, it has such a low prefactor that it is the least important of the major computational steps in this size regime.

The costs of the formation of J1 and K1 (the unprojected direct and exchange integrals defined in eqs 24 and 25) are summarized in Table 2. None of these steps should scale worse

Table 2. Theoretical and Actual Scaling for the Formation of J1 and K1^a

Component	Memory doubles	Scaling	
		Predicted	Observed
$(\phi_i \psi_a \chi_\mu \chi_\nu)$	$NO nv$	$NO n^3$	2.16
$(\phi_i \psi_a \phi_j \chi_\nu)$	$O^2 nv$	$O^2 n^2 v$	1.99
$(\phi_i \psi_a \phi_j \psi_b)$	$O^2 v^2$	$O^2 n v^2$	1.91
J1 Total	M^2	M^2	2.19
$(\overline{\phi_i \chi_\mu} \psi_a \chi_\nu)$	$(NO)nv$	$(NN)n^2 o$	2.89
$(\overline{\phi_i \phi_j} \psi_a \chi_\nu)$	$(OO)nv$	$(OO)n^2 v$	1.96
$(\overline{\phi_i \chi_\mu} \psi_a \chi_\nu)$	$(OO)v^2$	$(OO)n v^2$	2.00
K1 Total	(MM)	(MM)	2.88

^aCapital letters scale with the size of the system; lowercase letters are constant and are based on the identity of the fragments. N is the number of basis functions, O is the number of occupied orbitals, V is the number of virtual orbitals, and M is the system size. Parentheses indicate sparse matrix scaling: these scale quadratically for small systems and linearly otherwise.

than $O(M^2)$ with the system size, because we have designed our implementation to satisfy this criterion. J1 is most efficient

because the selection of significant ERIs can be done immediately at the shell-pair level, and, relative to K1, only one-quarter as many floating point operations are required per significant ERI. On the other hand, K1 technically has (NN) sparsity, meaning that only a linear number of significant matrix elements are required for sufficiently large systems. However, our present shell quartet selection algorithm is based on all *fragment pairs* and does not include screening based on fragment pairs that give vanishing K1 contributions; thus, it scales as $O(M^2)$.

The costs associated with forming the RI integrals and subsequently assembling the correction terms are given in Table 3.

Table 3. Theoretical and Actual Scaling for RI Integrals and Formation of Correction Terms J23, J4, K23, and K4^a

Component	Rate limiting step	Memory doubles	Scaling	
			Predicted	Observed
$(\chi^Q \chi^P)$	matrix inversion	X^2	X^3	2.82
$(\phi_i \phi_j \chi_P)$	$(\chi_\mu \chi_\nu \chi_P)$	$(OO)X^*$	$(NN)X$	2.55
$(\phi_i \psi_a \chi_P)$	$(\chi_\mu \chi_\nu \chi_P)$	OVX^*	$(NN)X$	2.66
c_{kl}^P	$v^{PQ} v_{klQ}$	$(OO)X$	$(OO)X^2$	3.06
\mathcal{V}_{ijkl}	$c_{ij}^P v_{klP}$	$(OO)^2$	$(OO)^2 X$	3.25
\mathcal{V}_{iajk}^P	$v_{iaP} c_{jk}^P$	$OV(OO)$	$OV(OO)X$	3.10
\mathcal{V}_{jak}^P	$c_{ij}^P v_{akP}$	$OV O^2$	$OV(OO)X$	3.14
J23	$\mathcal{V}_{iajk} \cdot \sigma_b^k$	$O^2 v^2$	$OV(OO)v$	1.88
J4	$\sigma_a^k \cdot \mathcal{V}_{ijkl} \cdot \sigma_b^l$	$O^2 v^2$	$(OO)^2 v$	2.29
K23	$\mathcal{V}_{iajk} \cdot \sigma_b^k$	$O^2 v^2$	$(OO)Ov^2$	2.06
K4	$\sigma_a^k \cdot \mathcal{V}_{ijkl} \cdot \sigma_b^l$	$O^2 v^2$	$(OO)^2 v$	2.94

^aNotation is the same as in Table 2, with the addition of X , the number of auxiliary functions. Where multiple steps are involved, the most costly step is indicated. Asterisk (*) denotes that the full set of three-center integrals never exist in memory simultaneously, due to the batching scheme.

These are unavoidably third-order steps, and they are implemented as such, as observed in the timings. The most costly $O(M^3)$ steps are the formation of the RI integral terms v_{ijP} and v_{iaP} , as in Figure 5. Their cost could still be reduced by approximately a factor of 2, by reusing the $(\chi_\mu \chi_\nu | \chi_P)$ terms, and there may be additional prefactor reductions that are possible. These optimizations will not affect the overall scaling. Thus, we successfully created an algorithm for computing excited states of clusters, which scales as $O(M^3)$. We have applied this code for timing purposes in calculations on as many as 485 atoms and 5335 basis functions, to obtain 4850 excited states. We believe that explicit excited-state calculations of this scale have not yet been reported.

4.3. Size Dependence of the Excitation Spectrum of Helium Clusters. In the ground state, the superfluidic phase can be distinguished for clusters with greater than ~ 60 atoms.⁵¹ In addition, it is predicted that clusters in the regime of ~ 500 atoms begin displaying bulklike properties.⁸² Thus, clusters containing 10^2 – 10^3 atoms are particularly interesting as they span this boundary region where observable properties are likely

to be changing. Previous theoretical studies of excited states of helium were only able to utilize clusters with ≤ 25 atoms, because of the computational cost associated with the large number of excited states required.^{58,59,83}

The size dependence of the helium cluster excitation spectrum is an ideal pilot application for ALMO–CIS. Earlier work on the spectra of He_7 and He_{25} clusters produced results that compared very favorably with previous experiments, when the geometries of the ground-state clusters are optimized with MP2/6-311G.⁵⁸ In larger clusters, nuclear quantum effects become increasingly important and failure to account for them results in overstructured clusters. Here, we consider clusters an order of magnitude larger (e.g., He_{231}), where MP2 optimizations are impractical; thus, as the ground-state structures are not critical to demonstrate the utility of ALMO–CIS, the cluster sampling was done with classical dynamics. For this paper, all geometries were obtained using the OPTIMIZE program in TINKER⁸⁴ after randomly perturbing an initial structure with atoms that are regularly spaced 4 Å apart. A He–He Lennard-Jones potential with $r_0 = 3.6$ Å and $\epsilon_0 = 0.05$ K was used for cluster optimization (note, bulk interatomic spacing in helium clusters is 3.6 Å). Since a tight optimization neglecting zero-point energy will give a highly ordered cluster, we used a loose convergence criterion to obtain randomized structures with spacing similar to the known He–He separations in solids and clusters. This should be sufficient for the qualitative study of size-dependent effects; further studies on the states of very large helium clusters are in progress, which account for nuclear effects.

The calculated spectra are shown in Figure 6. It is immediately evident that there are indeed strong size-dependent effects on the

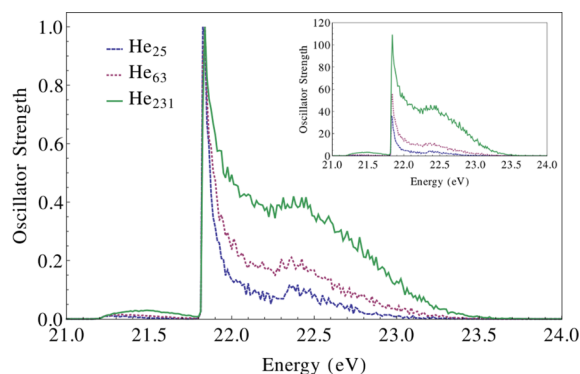


Figure 6. Calculated absorption spectra for He_{231} (solid green line), He_{63} (dotted purple line), and He_{25} (dashed blue line) at the ALMO–CIS level of theory, as a function of excitation energy (eV). In the main figure, the spectra are scaled so that the maximum peak height for each size cluster is 1, while the inset shows the unscaled spectrum.

absorption spectra. The first effect is an increase in oscillator strength contained in the band, which reflects the number of states in the manifold and increases linearly with size of the cluster. The second effect, also related to the oscillator strength, is the emergence of intensity borrowing in the $2s$ manifold as the cluster size increases. This reflects increased mixing with $2p$ states.

The most interesting size-dependent effects on the absorption spectrum are in the $2p$ band, where the width of the manifold increases noticeably with cluster size. In addition, the median of the oscillator strength shifts from the red edge of the manifold

in the small He_{25} cluster toward the middle by He_{231} . This unambiguously confirms the assignment of primarily “bulk” character to the states that lie toward the blue end of the manifold, versus those of “surface” character, which lie toward the red end of the manifold. The effects of increasing size are primarily due to the increasing importance of the bulklike states. In the 62- and 231-atom clusters, which contain the highest percentage of bulk states, a hump can be seen clearly forming near 22.4 eV that can be attributed to states on the interior of the cluster.

From section 4.1, we recall that the main ALMO–CIS error is the exaggerated bandwidth of the manifold, with the states on the blue edge increasingly overestimated. It is also possible that this effect increases with the size of the cluster, but since standard CIS cannot be reasonably run on the large clusters with enough states to explore the blue edge, we must leave this issue as an open question. The other result from our tests of ALMO–CIS vs CIS reported in section 4.1 was that neglect of the short-range charge transfer terms leads to an overall underestimate of oscillator strength, which likely becomes more important toward the blue edge as CT contributions become less negligible (although most likely still small).

5. CONCLUSIONS

Computations on homogeneous atomic and molecular clusters require large numbers of excited states to describe the broadening of atomic or molecular excitations into the bands associated with cluster, which gradually evolve toward the bulk limit. This need for many states makes conventional excited-state methods particularly costly for such applications. To address this problem, we have developed a physically motivated local variant of configuration interaction with single substitutions (CIS), which retains only intrafragment single excitations. We use the absolutely localized molecular orbitals (ALMOs) to describe occupied and virtual levels of the cluster, and thus term our fragment-localized method as ALMO–CIS. ALMO–CIS is physically appropriate for homogeneous clusters composed of atoms or molecules with high ionization potentials and low or negative electron affinities, as this combination minimizes the importance of the neglected charge-transfer terms.

The main conclusions of our work developing, implementing, testing, and applying the ALMO–CIS model are as follows:

(A) Formal Scaling. Complete construction and diagonalization of the ALMO–CIS Hamiltonian for all eigenvalues and eigenstates scales no worse than $O(M^3)$ with the number of atoms or molecules (M) in the cluster. By contrast, conventional CIS for all states scales as $O(M^6)$.

(B) Accuracy for Helium Cluster Absorption Spectra. Testing against full CIS for He_{25} absorption spectra shows good qualitative agreement for the full spectrum, and excellent quantitative agreement at the red edge of the $2s$ and $2p$ manifolds. ALMO–CIS systematically overestimates the excitation energies, with the error gradually increasing to its largest values at the blue edge of the $2p$ manifold, which can be corrected, when needed. When comparing ALMO–CIS to standard CIS, there is a clear decrease in total oscillator strength; however, the relative strength across the band is reasonably conserved, and the trend with increasing cluster size is consistent.

(C) Numerical Performance. We have successfully formulated and implemented an algorithm that is operationally $O(M^3)$ up to the largest cluster tested (485 atoms), and permits these

calculations with 4850 excited states and 5335 basis functions on workstation class computers.

(D) Application to Helium Cluster Absorption Spectra. As a pilot application, we evaluated the size dependence of absorption spectra of helium clusters and observed a variety of interesting effects that are qualitatively similar to trends seen experimentally. These include an increase in the intensity of the region corresponding to bulk-like states relative to the surface states, as well as a broadening of the primary peak.

(E) Further Possibilities. The ALMO–CIS model could benefit from a variety of improvements. Most important is some type of diagnostic or correction for the role of the neglected charge transfer (CT) configurations. Such differences also potentially yield physical insight into the role of CT in excited states. Also, dynamic correlation is missing, and might be reincorporated either by extending the model to time-dependent density functional theory, or incorporating wave-function-based correlation.

■ ASSOCIATED CONTENT

■ Supporting Information

The Supporting Information is available free of charge on the ACS Publications website at DOI: [10.1021/acs.jctc.5b00703](https://doi.org/10.1021/acs.jctc.5b00703).

Full derivation of the matrix elements and resolution of the identity corrections (PDF)

■ AUTHOR INFORMATION

Corresponding Author

*E-mail: mhg@cchem.berkeley.edu.

Present Address

§Materials Sciences Division, Lawrence Berkeley National Laboratory.

Notes

The authors declare the following competing financial interest(s): Yihan Shao and Martin Head-Gordon are part owners of Q-Chem, Inc.

■ ACKNOWLEDGMENTS

This work was supported by the Director, Office of Science, Office of Basic Energy Sciences, Chemical Sciences Division of the U.S. Department of Energy, under Contract No. DEAC02-05CH11231.

■ REFERENCES

- (1) Serrano-Andrés, L.; Merchán, M. J. *Mol. Struct.: THEOCHEM* **2005**, 729, 99–108.
- (2) Dreuw, A. *ChemPhysChem* **2006**, 7, 2259–2274.
- (3) Dreuw, A.; Head-Gordon, M. *Chem. Rev.* **2005**, 105, 4009–4037.
- (4) Casida, M. E.; Huix-Rotllant, M. *Annu. Rev. Phys. Chem.* **2012**, 63, 287–323.
- (5) Cai, Z.-L.; Sendt, K.; Reimers, J. R. *J. Chem. Phys.* **2002**, 117, 5543–5549.
- (6) Grimme, S.; Parac, M. *ChemPhysChem* **2003**, 4, 292–295.
- (7) Dreuw, A.; Head-Gordon, M. *J. Am. Chem. Soc.* **2004**, 126, 4007–4016.
- (8) Niehaus, T. A.; March, N. H. *Theor. Chem. Acc.* **2010**, 125, 427–432.
- (9) Foresman, J. B.; Head-Gordon, M.; Pople, J. A.; Frisch, M. J. *J. Phys. Chem.* **1992**, 96, 135–149.
- (10) Hirata, S.; Head-Gordon, M. *Chem. Phys. Lett.* **1999**, 314, 291–299.
- (11) Head-Gordon, M.; Rico, R.; Oumi, M.; Lee, T. *Chem. Phys. Lett.* **1994**, 219, 21–29.
- (12) Head-Gordon, M.; Oumi, M.; Maurice, D. *Mol. Phys.* **1999**, 96, 593–602.
- (13) Christiansen, O.; Koch, H.; Jørgensen, P. *Chem. Phys. Lett.* **1995**, 243, 409–418.
- (14) Stanton, J. F.; Gauss, J.; Ishikawa, N.; Head-Gordon, M. *J. Chem. Phys.* **1995**, 103, 4160–4174.
- (15) Krylov, A. I. *Annu. Rev. Phys. Chem.* **2008**, 59, 433–462.
- (16) Rhee, Y.-M.; Head-Gordon, M. *J. Phys. Chem. A* **2007**, 111, 5314–5326.
- (17) Casanova, D.; Rhee, Y. M.; Head-Gordon, M. *J. Chem. Phys.* **2008**, 128, 164106.
- (18) Roos, B. O.; Taylor, P. R.; Siegbahn, P. E. M. *Chem. Phys.* **1980**, 48, 157–173.
- (19) Page, C. S.; Olivucci, M. J. *Comput. Chem.* **2003**, 24, 298–309.
- (20) Casanova, D.; Head-Gordon, M. *Phys. Chem. Chem. Phys.* **2009**, 11, 9779–9790.
- (21) Bell, F.; Zimmerman, P. M.; Casanova, D.; Goldey, M.; Head-Gordon, M. *Phys. Chem. Chem. Phys.* **2013**, 15, 358–366.
- (22) Mayhall, N. J.; Head-Gordon, M. *J. Chem. Phys.* **2014**, 141, 044112.
- (23) Kohn, W. *Phys. Rev. Lett.* **1996**, 76, 3168–3171.
- (24) White, C. A.; Johnson, B. G.; Gill, P. M. W.; Head-Gordon, M. *Chem. Phys. Lett.* **1996**, 253, 268–278.
- (25) Ochsenfeld, C.; White, C. A.; Head-Gordon, M. *J. Chem. Phys.* **1998**, 109, 1663–1669.
- (26) Scuseria, G. E. *J. Phys. Chem. A* **1999**, 103, 4782–4790.
- (27) Goedecker, S. *Rev. Mod. Phys.* **1999**, 71, 1085–1123.
- (28) Baer, R.; Head-Gordon, M. *Phys. Rev. Lett.* **1997**, 79, 3962–3965.
- (29) Yam, C. Y.; Zhang, Q.; Wang, F.; Chen, G. H. *Chem. Soc. Rev.* **2012**, 41, 3821–3838.
- (30) Kjaergaard, T.; Jørgensen, P.; Olsen, J.; Coriani, S.; Helgaker, T. J. *Chem. Phys.* **2008**, 129, 054106.
- (31) Tretiak, S.; Isborn, C. M.; Niklasson, A. M. N.; Challacombe, M. J. *Chem. Phys.* **2009**, 130, 054111.
- (32) Li, Q. X.; Li, Q. K.; Shuai, Z. G. *Synth. Met.* **2008**, 158, 330–335.
- (33) Miura, M.; Aoki, Y. *J. Comput. Chem.* **2009**, 30, 2213–2230.
- (34) Miura, M.; Aoki, Y. *Mol. Phys.* **2010**, 108, 205–210.
- (35) Wu, F. Q.; Liu, W. J.; Zhang, Y.; Li, Z. D. *J. Chem. Theory Comput.* **2011**, 7, 3643–3660.
- (36) Tsuchiya, T.; Shrestha, K.; Jakubikova, E. J. *Chem. Theory Comput.* **2013**, 9, 3350–3363.
- (37) Svensson, M.; Humbel, S.; Froese, R. D. J.; Matsubara, T.; Sieber, S.; Morokuma, K. *J. Phys. Chem.* **1996**, 100, 19357–19363.
- (38) Senn, H. M.; Thiel, W. *Angew. Chem., Int. Ed.* **2009**, 48, 1198–1229.
- (39) Li, X.; Chung, L. W.; Morokuma, K. In *Computational Methods for Large Systems: Electronic Structure Approaches for Biotechnology and Nanotechnology*; Reimers, J. R., Ed.; John Wiley & Sons, Inc.: Hoboken, NJ, 2011; Chapter 12, pp 397–433.
- (40) Mata, R. A.; Stoll, H. *J. Chem. Phys.* **2011**, 134, 034122.
- (41) Fedorov, D. G.; Nagata, T.; Kitaura, K. *Phys. Chem. Chem. Phys.* **2012**, 14, 7562–7577.
- (42) Ikegami, T.; Ishida, T.; Fedorov, D. G.; Kitaura, K.; Inadomi, Y.; Umeda, H.; Yokokawa, M.; Sekiguchi, S. *J. Comput. Chem.* **2009**, 31, 447–454.
- (43) Grimme, S. *J. Chem. Phys.* **2013**, 138, 244104.
- (44) Risthaus, T.; Hansen, A.; Grimme, S. *Phys. Chem. Chem. Phys.* **2014**, 16, 14408–14419.
- (45) Liu, J.; Herbert, J. M. *J. Chem. Phys.* **2015**, 143, 034106.
- (46) Helmich, B.; Hättig, C. *J. Chem. Phys.* **2011**, 135, 214106.
- (47) Helmich, B.; Hättig, C. *J. Chem. Phys.* **2013**, 139, 084114.
- (48) Jortner, J. Z. *Phys. D: At., Mol. Clusters* **1992**, 24, 247–275.
- (49) Castleman, A. W., Jr.; Bowen, K. H., Jr. *J. Phys. Chem.* **1996**, 100, 12911–12944.
- (50) Bartell, L. S. *Annu. Rev. Phys. Chem.* **1998**, 49, 43–72.
- (51) Grebenev, S.; Toennies, J. P.; Vilesov, A. F. *Science* **1998**, 279, 2083–2086.
- (52) Stienkemeier, F.; Vilesov, A. F. *J. Chem. Phys.* **2001**, 115, 10119.

- (53) Toennies, J. P.; Vilesov, A. F. *Angew. Chem., Int. Ed.* **2004**, *43*, 2622–2648.
- (54) Choi, M. Y.; Doublerly, G. E.; Falconer, T. M.; Lewis, W. K.; Lindsay, C. M.; Merritt, J. M.; Stiles, P. L.; Miller, R. E. *Int. Rev. Phys. Chem.* **2006**, *25*, 15–75.
- (55) Wang, C. C.; Kornilov, O.; Gessner, O.; Kim, J. H.; Peterka, D. S.; Neumark, D. M. *J. Phys. Chem. A* **2008**, *112*, 9356–9365.
- (56) Joppien, M.; Karnbach, R.; Möller, T. *Phys. Rev. Lett.* **1993**, *71*, 2654–2657.
- (57) Mudrich, M.; Stienkemeier, F. *Int. Rev. Phys. Chem.* **2014**, *33*, 301–339.
- (58) Closser, K. D.; Head-Gordon, M. *J. Phys. Chem. A* **2010**, *114*, 8023–8032.
- (59) Closser, K. D.; Gessner, O.; Head-Gordon, M. *J. Chem. Phys.* **2014**, *140*, 134306.
- (60) Khaliullin, R. Z.; Head-Gordon, M.; Bell, A. T. *J. Chem. Phys.* **2006**, *124*, 204105.
- (61) Stoll, H.; Wagenblast, G.; Preuss, H. *Theor. Chim. Acta* **1980**, *57*, 169–178.
- (62) Cullen, J. *Int. J. Quantum Chem.* **1991**, *40*, 193–207.
- (63) Gianinetti, E.; Raimondi, M.; Tornaghi, E. *Int. J. Quantum Chem.* **1996**, *60*, 157–166.
- (64) Nagata, T.; Takahashi, O.; Saito, K.; Iwata, S. *J. Chem. Phys.* **2001**, *115*, 3553–3560.
- (65) Mo, Y. R.; Gao, J. L.; Peyerimhoff, S. D. *J. Chem. Phys.* **2000**, *112*, 5530–5538.
- (66) Khaliullin, R. Z.; Cobar, E. A.; Lochan, R. C.; Bell, A. T.; Head-Gordon, M. *J. Phys. Chem. A* **2007**, *111*, 8753–8765.
- (67) Khaliullin, R. Z.; Bell, A. T.; Head-Gordon, M. *J. Chem. Phys.* **2008**, *128*, 184112.
- (68) Horn, P. R.; Sundstrom, E. J.; Baker, T. A.; Head-Gordon, M. *J. Chem. Phys.* **2013**, *138*, 134119.
- (69) Head-Gordon, M.; Maslen, P. E.; White, C. A. *J. Chem. Phys.* **1998**, *108*, 616–625.
- (70) Head-Gordon, M.; Lee, M. S.; Maslen, P. E.; Van Voorhis, T. A.; Gwaltney, S. R. In *Modern Methods and Algorithms of Quantum Chemistry*; Grotendorst, J., Ed.; John von Neumann Institute for Computing (NIC) Series, Vol. 3; John von Neumann Institute for Computing: Jülich, Germany, 2000; pp 593–638.
- (71) Shao, Y.; Molnar, L. F.; Jung, Y.; Kussmann, J.; Ochsenfeld, C.; Brown, S. T.; Gilbert, A. T. B.; Slipchenko, L. V.; Levchenko, S. V.; O'Neill, D. P.; DiStasio, R. A., Jr.; Lochan, R. C.; Wang, T.; Beran, G. J. O.; Besley, N. A.; Herbert, J. M.; Lin, C. Y.; Van Voorhis, T.; Chien, S. H.; Sodt, A.; Steele, R. P.; Rassolov, V. A.; Maslen, P. E.; Korambath, P. P.; Adamson, R. D.; Austin, B.; Baker, J.; Byrd, E. F. C.; Dachsels, H.; Doerksen, R. J.; Dreuw, A.; Dunietz, B. D.; Dutoi, A. D.; Furlani, T. R.; Gwaltney, S. R.; Heyden, A.; Hirata, S.; Hsu, C.-P.; Kedziora, G.; Khaliullin, R. Z.; Klunzinger, P.; Lee, A. M.; Lee, M. S.; Liang, W.; Lotan, I.; Nair, N.; Peters, B.; Proynov, E. I.; Pieniazek, P. A.; Rhee, Y. M.; Ritchie, J.; Rosta, E.; Sherrill, C. D.; Simmonett, A. C.; Subotnik, J. E.; Woodcock, H. L., III; Zhang, W.; Bell, A. T.; Chakraborty, A. K.; Chipman, D. M.; Keil, F. J.; Warshel, A.; Hehre, W. J.; Schaefer, H. F., III; Kong, J.; Krylov, A. I.; Gill, P. M. W.; Head-Gordon, M. *Phys. Chem. Chem. Phys.* **2006**, *8*, 3172–3191.
- (72) Shao, Y.; Gan, Z.; Epifanovsky, E.; Gilbert, A. T.; Wormit, M.; Kussmann, J.; Lange, A. W.; Behn, A.; Deng, J.; Feng, X.; Ghosh, D.; Goldey, M.; Horn, P. R.; Jacobson, L. D.; Kaliman, I.; Khaliullin, R. Z.; Kus, T.; Landau, A.; Liu, J.; Proynov, E. I.; Rhee, Y. M.; Richard, R. M.; Rohrdanz, M. A.; Steele, R. P.; Sundstrom, E. J.; Woodcock, H. L.; Zimmerman, P. M.; Zuev, D.; Albrecht, B.; Alguire, E.; Austin, B.; Beran, G. J. O.; Bernard, Y. A.; Berquist, E.; Brandhorst, K.; Bravaya, K. B.; Brown, S. T.; Casanova, D.; Chang, C.-M.; Chen, Y.; Chien, S. H.; Closser, K. D.; Crittenden, D. L.; Didenhofen, M.; DiStasio, R. A.; Do, H.; Dutoi, A. D.; Edgar, R. G.; Fatehi, S.; Fusti-Molnar, L.; Ghysels, A.; Golubeva-Zadorozhnaya, A.; Gomes, J.; Hanson-Heine, M. W.; Harbach, P. H.; Hauser, A. W.; Hohenstein, E. G.; Holden, Z. C.; Jagau, T.-C.; Ji, H.; Kaduk, B.; Khistyayev, K.; Kim, J.; Kim, J.; King, R. A.; Klunzinger, P.; Koskenkov, D.; Kowalczyk, T.; Krauter, C. M.; Lao, K. U.; Laurent, A.; Lawler, K. V.; Levchenko, S. V.; Lin, C. Y.; Liu, F.; Livshits,
- E.; Lochan, R. C.; Luenser, A.; Manohar, P.; Manzer, S. F.; Mao, S.-P.; Mardirossian, N.; Marenich, A. V.; Maurer, S. A.; Mayhall, N. J.; Neuscamman, E.; Oana, C. M.; Olivares-Amaya, R.; O'Neill, D. P.; Parkhill, J. A.; Perrine, T. M.; Peverati, R.; Prociuk, A.; Rehn, D. R.; Rosta, E.; Russ, N. J.; Sharada, S. M.; Sharma, S.; Small, D. W.; Sodt, A.; Stein, T.; Stück, D.; Su, Y.-C.; Thom, A. J.; Tsuchimochi, T.; Vanovschi, V.; Vogt, L.; Vydrov, O.; Wang, T.; Watson, M. A.; Wenzel, J.; White, A.; Williams, C. F.; Yang, J.; Yeganeh, S.; Yost, S. R.; You, Z.-Q.; Zhang, I. Y.; Zhang, X.; Zhao, Y.; Brooks, B. R.; Chan, G. K.; Chipman, D. M.; Cramer, C. J.; Goddard, W. A.; Gordon, M. S.; Hehre, W. J.; Klamt, A.; Schaefer, H. F.; Schmidt, M. W.; Sherrill, C. D.; Truhlar, D. G.; Warshel, A.; Xu, X.; Aspuru-Guzik, A.; Baer, R.; Bell, A. T.; Besley, N. A.; Chai, J.-D.; Dreuw, A.; Dunietz, B. D.; Furlani, T. R.; Gwaltney, S. R.; Hsu, C.-P.; Jung, Y.; Kong, J.; Lambrecht, D. S.; Liang, W.; Ochsenfeld, C.; Rassolov, V. A.; Slipchenko, L. V.; Subotnik, J. E.; Van Voorhis, T.; Herbert, J. M.; Krylov, A. I.; Gill, P. M.; Head-Gordon, M. *Mol. Phys.* **2015**, *113*, 184–215.
- (73) Davidson, E. R. *J. Comput. Phys.* **1975**, *17*, 87–94.
- (74) Häser, M.; Ahlrichs, R. *J. Comput. Chem.* **1989**, *10*, 104–111.
- (75) Kussmann, J.; Ochsenfeld, C. *J. Chem. Phys.* **2013**, *138*, 134114.
- (76) Weigend, F.; Häser, M.; Patzelt, H.; Ahlrichs, R. *Chem. Phys. Lett.* **1998**, *294*, 143–152.
- (77) Reine, S.; Tellgren, E.; Krapp, A.; Kjaergaard, T.; Helgaker, T.; Jansik, B.; Host, S.; Salek, P. *J. Chem. Phys.* **2008**, *129*, 104101.
- (78) Gill, P. M. W.; Pople, J. A. *Int. J. Quantum Chem.* **1991**, *40*, 753–772.
- (79) Gill, P. M. W. *Adv. Quantum Chem.* **1994**, *25*, 141–205.
- (80) Gill, P. M. W.; Gilbert, A. T. B.; Adams, T. R. *J. Comput. Chem.* **2000**, *21*, 1505–1510.
- (81) Ochsenfeld, C.; White, C. A.; Head-Gordon, M. *J. Chem. Phys.* **1998**, *109*, 1663–1669.
- (82) von Haeften, K.; Laarmann, T.; Wabnitz, H.; Möller, T.; Fink, K. *J. Phys. Chem. A* **2011**, *115*, 7316–7326.
- (83) von Haeften, K.; Fink, K. *Eur. Phys. J. D* **2007**, *43*, 121–124.
- (84) Ponder, J. W. *TINKER Molecular Modeling Package, V7.1*; 2015.